Global phenomenological optical model potential for nucleon-actinide reactions at energies up to 300 MeV

Yinlu Han,[1,*] Yongli Xu,[1,2] Haiying Liang,[1] Hairui Guo,[1] and Qingbiao Shen[1]
[1]*China Institute of Atomic Energy, Post Office Box 275(41), Beijing 102413, People's Republic of China*
[2]*College of Physics and Electronic Science, Shanxi Datong University, Datong 037009, People's Republic of China*
(Received 23 November 2009; published 25 February 2010)

A set of new global phenomenological optical model potential parameters for the actinide region with incident nucleon energies from 1 keV up to 300 MeV is obtained. They are based on a smooth, unique functional form for the energy dependence of the potential depths and on physically constrained geometry parameters. The available experimental data including the neutron total cross sections, nonelastic cross sections, elastic scattering cross sections, elastic scattering angular distributions, and proton reaction cross sections and elastic scattering angular distributions of ^{232}Th and ^{238}U are used. The new nucleon global optical model potential parameters obtained are analyzed and used to analyze the experimental data of nucleon-actinide reactions. It is found that the present form of the global optical model potential could reproduce both the neutron and the proton experimental data.

DOI: 10.1103/PhysRevC.81.024616 PACS number(s): 24.10.Ht, 25.40.Cm, 25.40.Dn, 25.40.Fq

I. INTRODUCTION

The optical model has a significant impact on many branches of nuclear reaction physics. The central assumption of this model is that the complicated interaction between an incident particle and a nucleus can be represented by a complex mean-field potential, which divides the reaction flux into one part covering shape elastic scattering and another describing all competing nonelastic channels. Solving the Schrödinger equation with this complex potential can give the elastic scattering angular distribution and total reaction cross sections of nucleon-induced reactions. An important feature of a good optical model potential is that it can be used to reliably calculate reaction cross sections and elastic scattering angular distribution in some energies and nuclide regions in which no experimental measurement data exist. Moreover, the quality of several derived quantities that are provided by the optical model has an important impact on the evaluation of the various nonelastic channels. Well-known examples are the related transmission coefficients that enter the statistical model of compound nucleus evaporation and the distorted wave functions that are used for the description of direct inelastic scattering to discrete states as well as in evaluations of multistep direct transitions to the continuum states. The reaction cross sections calculated with the optical model are important for the evaporation part of intranuclear cascade models and also for semiclassical pre-equilibrium models. All these nuclear models for the nonelastic channels rely on various other ingredients, such as discrete level schemes, level densities, γ-ray strength functions, and fission barriers, etc. The uncertainties in those quantities are added to the total uncertainty term of the calculated results. Therefore, it is crucial that the optical model potentials for such kinds of nuclear model calculations must be adequately determined.

In addition, knowledge of accurate cross sections of a number of reactions (e.g., total, nonelastic, fission) between neutrons and actinides is crucially important for designing various reactor systems. In the accelerator-driven system (ADS) of radioactive waste transmutation and energy generation, the nuclear reaction data are needed for both neutrons and protons as projectiles up to several hundred MeV. The optical model is one of the fundamental theoretical tools that provide the basis of nuclear reaction data analysis and various cross sections.

Koning and Delaroche [1] gave phenomenological local and global optical model potentials for neutrons and protons with incident energies from 1 keV up to 200 MeV for (near-)spherical nuclides in the mass range $24 \leqslant A \leqslant 209$, in which the appropriate experimental data were available. These potentials are based on a smooth, unique functional form for the energy dependence of the potential depths and on physically constrained geometry parameters.

The purpose of this article is to derive a set of nucleon phenomenological global optical model potential parameters for the actinide in the charge number range $89 \leqslant Z \leqslant 100$ and the mass range $220 \leqslant A \leqslant 260$, based on the appropriate experimental data including the neutron total cross sections, nonelastic cross sections, elastic scattering cross sections, elastic scattering angular distributions, and proton reaction cross sections and elastic scattering angular distributions of ^{232}Th and ^{238}U at incident nucleon energies up to 300 MeV. The new nucleon global optical model potential parameters obtained are analyzed and used to calculate cross sections and elastic scattering angular distribution of nucleon-actinide reactions. The calculated results by using the global optical model potential are compared with the neutron and proton experimental data. The inelastic scattering angular distributions of neutron- and proton-induced reactions are also calculated and analyzed by global optical model potentials.

The article is structured as follows. Section II provides a description of the optical model formalism and the forms of the energy and radial dependencies of the real, imaginary, and spin-orbit potentials. Section III describes the calculated

*hanyl@ciae.ac.cn

 ©2010 The American Physical Society

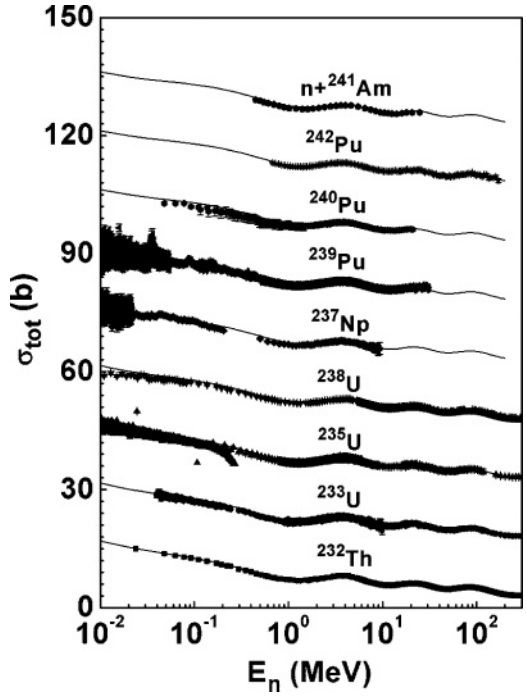

FIG. 1. Calculated total cross section (solid line) compared with experimental data [6–32] for $n + {}^{232}$Th, ^{233,235,238}U, ^{237}Np, ^{239,240,242}Pu, and ^{241}Am reactions. The results are offset by factors of $\times 2$, $\times 3$, $\times 4, \ldots, \times 9$.

method and gives the set of nucleon phenomenological global optical model potential parameters. Section IV is the comparison and analysis of the calculated results and experimental data. Finally, Sec. V contains our conclusions.

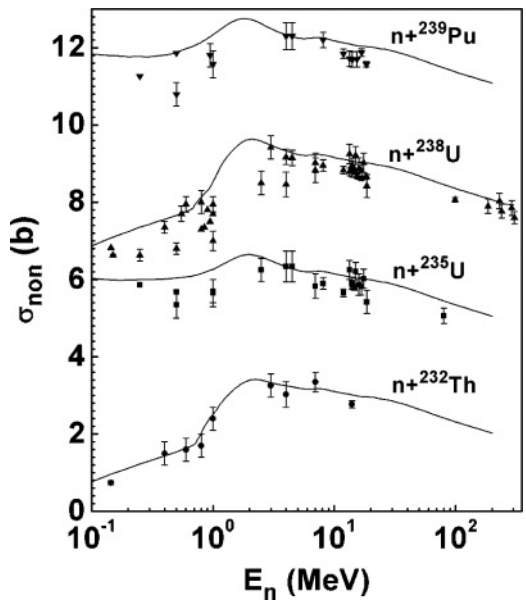

FIG. 2. Calculated nonelastic scattering cross sections (solid line) compared with experimental data for $n + {}^{232}$Th, ^{235,238}U, and ^{239}Pu reactions. The results are offset by factors of $+3$, $+6$, and $+9$.

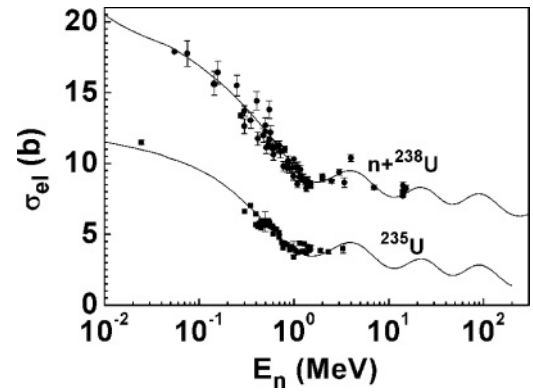

FIG. 3. Calculated elastic scattering cross sections (solid line) compared with experimental data for $n + {}^{235,238}$U reactions. The results are offset by factors of $+5$.

II. THE OPTICAL MODEL POTENTIALS

The optical model potentials considered here are Woods-Saxon form for the real part, Woods-Saxon form and derivative Woods-Saxon form for the imaginary parts, respectively corresponding to the volume and surface absorption, and the Thomas form for the spin-orbit part. The analytical expression of the phenomenological optical model potential form is supposed to be dependent on nuclear radius r, nuclear

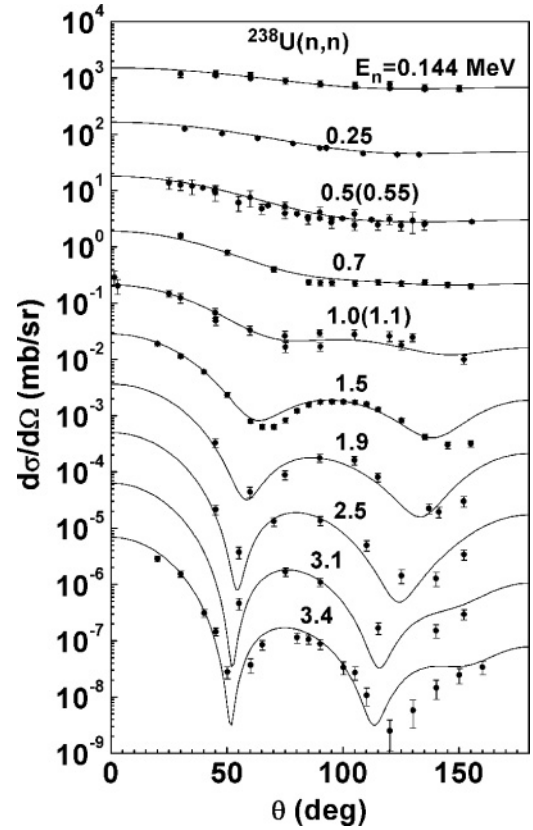

FIG. 4. Calculated elastic scattering angular distributions (solid line) compared with experimental data [35–37] for $n + {}^{238}$U reactions. The results are offset by factors of $\times 10$, $\times 10^2$, $\times 10^3, \ldots$.

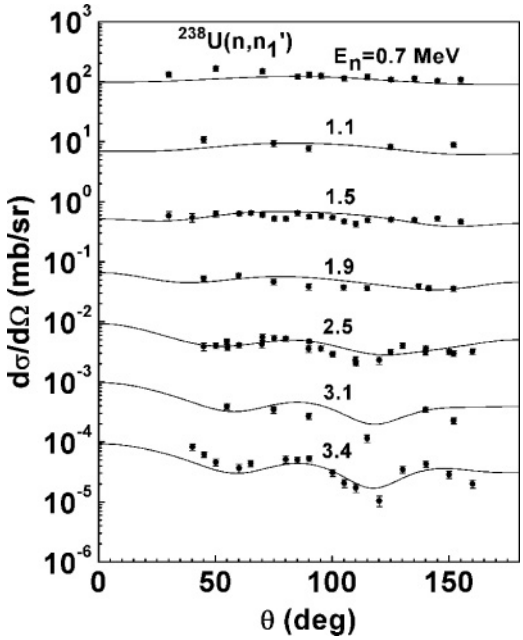

FIG. 5. Calculated inelastic scattering angular distributions of the first excited state (solid line) compared with experimental data [36,37] for $n + {}^{238}$U reactions. The results are offset by factors of $\times 10$, $\times 10^2$, $\times 10^3$, ...

diffuseness width a, target mass number A, charge number Z, neutron number N, and incident energy in laboratory system E. The optical potential formulas include some adjustable parameters that are decided by fitting the calculated cross sections and angular distributions with the experimental data. The Woods-Saxon form phenomenological optical potential is

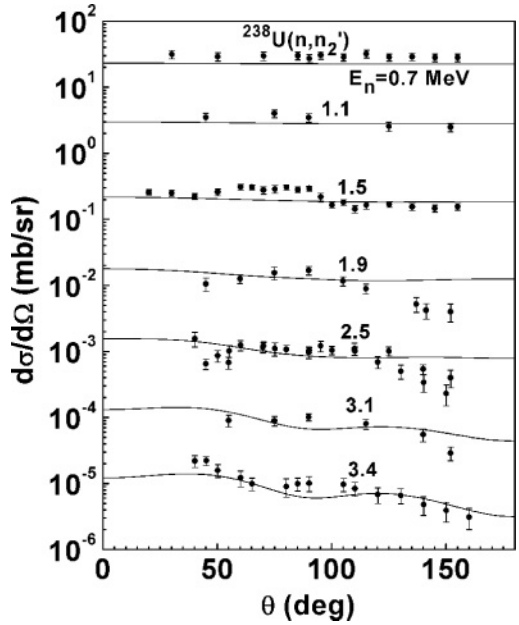

FIG. 6. Calculated inelastic scattering angular distributions of the second excited state (solid line) compared with experimental data [36,37] for $n + {}^{238}$U reactions. The results are offset by factors of $\times 10$, $\times 10^2$, $\times 10^3$, ...

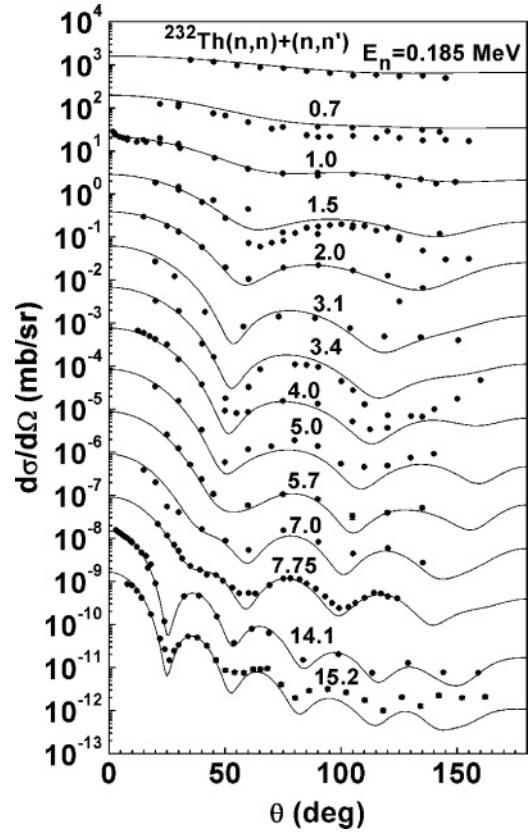

FIG. 7. Calculated elastic and inelastic scattering angular distributions of first, second, third, and fourth excited states (solid line) compared with experimental data [35–45] for $n + {}^{232}$Th reactions. The results are offset by factors of $\times 10$, $\times 10^2$, $\times 10^3$, ...

one of the universally used optical potentials. Its general form is as follows

$$V(r, E) = V_R(r, E) + i[W_S(r, E) + W_V(r, E)] + V_C(r) + V_{SO}(r)(\vec{s} \cdot \vec{l}), \quad (1)$$

where $V_R(r, E)$ is the real part potential, $W_S(r, E)$ and $W_V(r, E)$ are, respectively, the imaginary part potential of surface absorption and volume absorption, V_{SO} is the real part of the spin-orbit potential, $V_C(r)$ is the Coulomb potential, and $\vec{s}$ and $\vec{l}$ are spin and orbit angular momentum of the incident particle, respectively. The details of these terms can be expressed as follows.

The real part of the optical model potential is

$$V_R(r, E) = -\frac{V_R(E)}{1 + \exp[(r - R_R)/a_R]}. \quad (2)$$

The imaginary part of the surface absorption of the optical model potential is

$$W_S(r, E) = -4W_S(E)\frac{\exp[(r - R_S)/a_S)]}{\{1 + \exp[(r - R_S)/a_S]\}^2}. \quad (3)$$

The imaginary part of the volume absorption of the optical model potential is

$$W_V(r, E) = -\frac{W_V(E)}{1 + \exp[(r - R_V)/a_V]}. \quad (4)$$

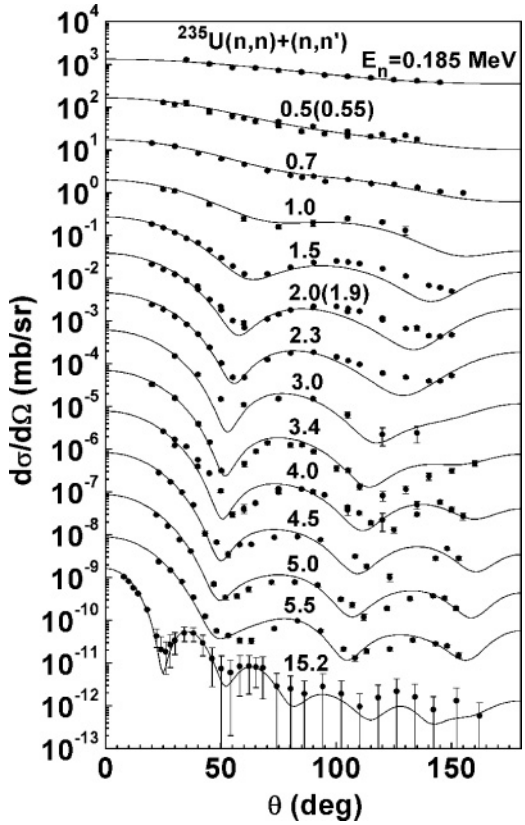

FIG. 8. Calculated elastic and inelastic scattering angular distributions of first, second, third, and fourth excited states (solid line) compared with experimental data [36,39,46–49] for $n + {}^{235}$U reactions. The results are offset by factors of $\times 10$, $\times 10^2$, $\times 10^3$, ...

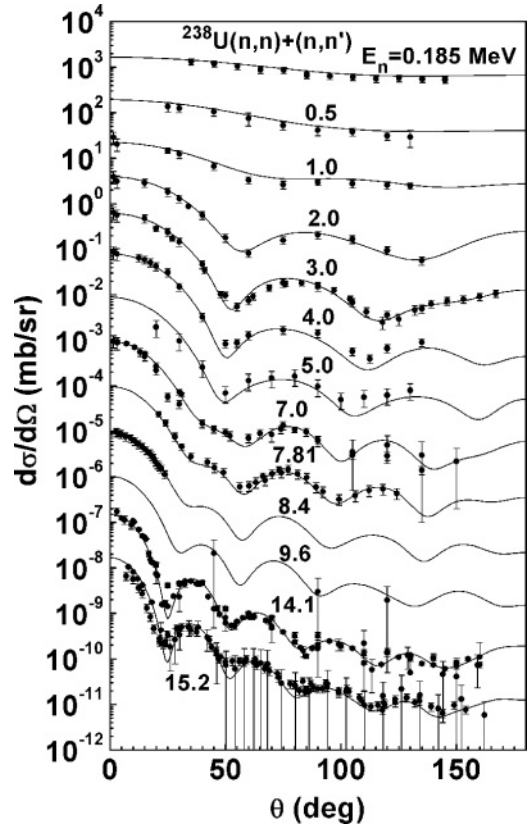

FIG. 9. Calculated elastic and inelastic scattering angular distributions of first, second, third, and fourth excited states (solid line) compared with experimental data [38,39,42,43,45,48,50–55] for $n + {}^{238}$U reactions. The results are offset by factors of $\times 10$, $\times 10^2$, $\times 10^3$, ...

The spin-orbit potential is

$$V_{\rm SO}(r) = -\lambda_\pi^2 \frac{V_{\rm SO}}{a_{\rm SO} r} \frac{\exp[(r - R_{\rm SO})/a_{\rm SO}]}{\{1 + \exp[(r - R_{\rm SO})/a_{\rm SO}]\}^2}. \quad (5)$$

The Coulomb potential that is taken from the electric field of a spherical homogeneous charge density nucleus with radius R_C is given by

$$V_C(r) = \begin{cases} \frac{zZe^2}{2R_C}\left(3 - \frac{r^2}{R_C^2}\right) & r < R_C. \\ \frac{zZe^2}{r} & r \geqslant R_C. \end{cases} \quad (6)$$

Here z is the charge number of the projectile. This term is zero for neutron as projectile ($z = 0.0$), and has a contribution for proton as projectile ($z = 1.0$).

The energy dependence of the potential depth is given by

$$V_R(E) = V_0 + V_1 E + V_2 E^2 + V_3 \frac{(N - Z)}{A}, \quad (7)$$

$$W_S(E) = \max\left\{0, W_0 + W_1 E + W_2 \frac{(N - Z)}{A}\right\}, \quad (8)$$

$$W_V(E) = \max\{0, U_0 + U_1 E + U_2 E^2\}. \quad (9)$$

The radii are given by

$$R_i = r_i A^{\frac{1}{3}}, \quad i = R, S, V, {\rm SO}, C. \quad (10)$$

Where r_R, r_S, r_V, $r_{\rm SO}$, and r_C are the radius of the real part, the surface absorption, the volume absorption, the spin-orbit couple, and the Coulomb potential, respectively.

The a_R, a_S, a_V, and $a_{\rm SO}$ mentioned in Eqs. (2)–(5) are the width of the real part, the surface absorption, the volume absorption, and the spin-orbit couple potential, respectively. λ_π is the Compton wavelength of pion, $\lambda_\pi^2 = 2.0$ fm^2.

The units of the potential V_R, W_S, W_V, and $V_{\rm SO}$ are in MeV; the lengths r_R, r_S, r_V, $r_{\rm SO}$, and r_V and a_R, a_S, a_V, and $a_{\rm SO}$ are in fm; and the energy E is in MeV.

The 20 parameters V_0, V_1, V_2, V_3, W_0, W_1, W_2, U_0, U_1, U_2, $V_{\rm SO}$, r_R, r_S, r_V, $r_{\rm SO}$, r_C, a_R, a_S, a_V, and $a_{\rm SO}$ can be adjusted. The parameters V_3, W_2, $V_{\rm SO}$, $r_{\rm SO}$, r_C, and $a_{\rm SO}$ are fixed and are taken from the work by Becchetti and Greenlees [2]. The 14 parameters are adjusted in the present work.

The Hauser-Feshbach theory with the width fluctuation correction is used to calculate the compound nucleus elastic scattering cross sections and angular distributions and the inelastic scattering cross sections and angular distributions at low incident nucleon energies.

The inelastic scattering cross sections and inelastic scattering angular distributions to low-lying states are important in nuclear theoretical calculations. The code DWUCK [3] with a distorted-wave Born approximation is used to calculate direct

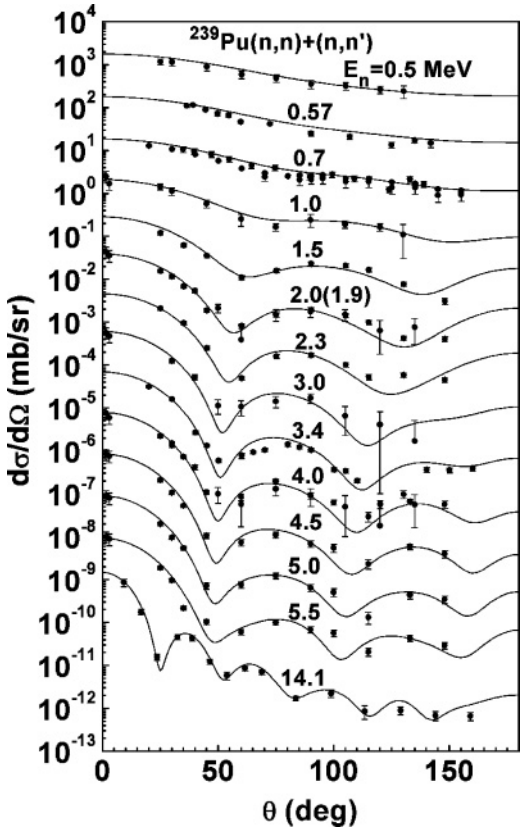

FIG. 10. Calculated elastic and inelastic scattering angular distributions of first, second, third, and fourth excited states (solid line) compared with experimental data [36,45,48,49,56,57] for $n + {}^{239}$Pu reactions. The results are offset by factors of $\times 10$, $\times 10^2$, $\times 10^3$, ...

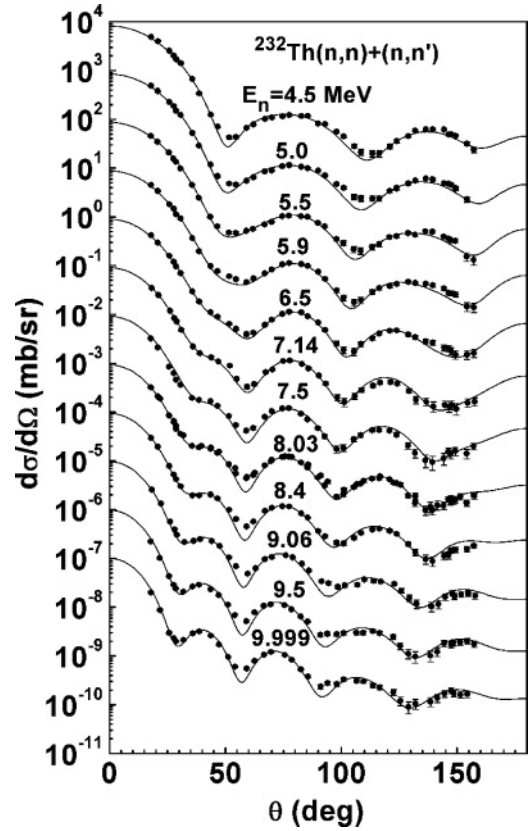

FIG. 11. Calculated elastic and inelastic scattering angular distributions of first, second, third, and fourth excited states (solid line) compared with experimental data [58] for $n + {}^{232}$Th reactions. The results are offset by factors of $\times 10$, $\times 10^2$, $\times 10^3$, ...

inelastic scattering cross sections and direct inelastic scattering angular distributions for excited states.

III. THE GLOBAL OPTICAL MODEL POTENTIAL PARAMETERS

The adjustment of the optical potential parameters is performed automatically with a computer program to minimize a quantity called χ^2, which represents the deviation of the calculated results from experimental values, that is,

$$\chi^2_{i,\mathrm{tot}} = \frac{1}{N_{i,\mathrm{tot}}} \sum_{j=1}^{N_{i,\mathrm{tot}}} \left[\frac{\sigma^T_{i,\mathrm{tot}}(j) - \sigma^E_{i,\mathrm{tot}}(j)}{\Delta\sigma^E_{i,\mathrm{tot}}(j)} \right]^2, \tag{11}$$

$$\chi^2_{i,\mathrm{ne}} = \frac{1}{N_{i,\mathrm{ne}}} \sum_{j=1}^{N_{i,\mathrm{ne}}} \left[\frac{\sigma^T_{i,\mathrm{ne}}(j) - \sigma^E_{i,\mathrm{ne}}(j)}{\Delta\sigma^E_{i,\mathrm{ne}}(j)} \right]^2, \tag{12}$$

$$\chi^2_{i,\mathrm{el}} = \frac{1}{N_{i,\mathrm{el}}} \sum_{j=1}^{N_{i,\mathrm{el}}} \frac{1}{K_{i,j,\mathrm{el}}} \sum_{k=1}^{K_{i,j,\mathrm{el}}} \left[\frac{\sigma^T_{i,j,\mathrm{el}}(\theta_{i,j,k}) - \sigma^E_{i,j,\mathrm{el}}(\theta_{i,j,k})}{\Delta\sigma^E_{i,j,\mathrm{el}}(\theta_{i,j,k})} \right]^2. \tag{13}$$

Where $N_{i,\mathrm{tot}}$, $N_{i,\mathrm{ne}}$, and $N_{i,\mathrm{el}}$ are the numbers of energy points for the experimental data of the total cross sections, nonelastic scattering cross sections, and elastic scattering angular distributions for the ith nucleus, respectively. $K_{i,j,\mathrm{el}}$ is the number of angles of the experimental data of elastic scattering angular distributions for the ith nucleus at jth energy point. The superscripts T and E represent the theoretical and experimental values, respectively; $\sigma_{i,\mathrm{tot}}(j)$ and $\sigma_{i,\mathrm{ne}}(j)$ are total and nonelastic cross sections for the ith nucleus at jth energy point; and there is no total cross section for proton projectile. $\sigma_{i,j,\mathrm{el}}(\theta_{i,j,k})$ is the elastic scattering angular distribution for the ith nucleus at jth energy point and kth outgoing angle; $\Delta\sigma$ is the experimental data error of the corresponding data. The χ^2 values given by Eqs. (11)–(13) are regarded as functions of the N adjustable optical potential parameters.

The program APMN [4] for automatically searching optimal optical potential parameters in the energy region $E \leqslant 300$ MeV by means of the improved fastest falling method [5] is further improved upon and used in the present work.

The experimental data of total, nonelastic, and elastic cross sections and elastic scattering angular distributions are collected and analyzed. The nucleus charge number range of $89 \leqslant Z \leqslant 100$, mass range of $220 \leqslant A \leqslant 260$, and incident nucleon energy up to 300 MeV are included. We started with ^{232}Th and ^{238}U because they are the only actinides for which the experimental data of total, nonelastic, and elastic cross sections and elastic scattering angular distributions for neutron projectile and the reaction cross sections and elastic scattering angular distributions for proton projectile can be found. We performed the analysis again in order to extract a

TABLE I. The global neutron and proton optical model potential parameters.

V_0	49.73099136	V_{SO}	6.2
V_1	−0.23824683	a_R	0.57523543
V_2	0.00019246	a_S	0.77411819
V_3	−24.0	a_V	0.30000000
W_0	9.54198456	a_{SO}	0.75
W_1	−0.02713984	r_R	1.26837850
W_2	−12.0	r_S	1.14190519
U_0	−0.30205852	r_V	1.35801959
U_1	0.08792425	r_{SO}	1.10
U_2	−0.00012181	r_C	1.25

set of global parameters based on as much experimental data of ^{232}Th and ^{238}U as possible. The optical model potential parameters obtained are given in Table I.

The real part potential and Coulomb potential of the optical model are used to describe elastic scattering angular distributions. The imaginary part potential of the optical model describes the total reaction cross sections. From Eqs. (2)–(10) and Table I we can see that the contribution of the real part potential [Eqs. (2) and (7)] decreases with increasing incident nucleon energy. The contribution of the imaginary part potential of the surface absorption [Eqs. (3) and (8)] decreases and the imaginary part potential of the volume absorption

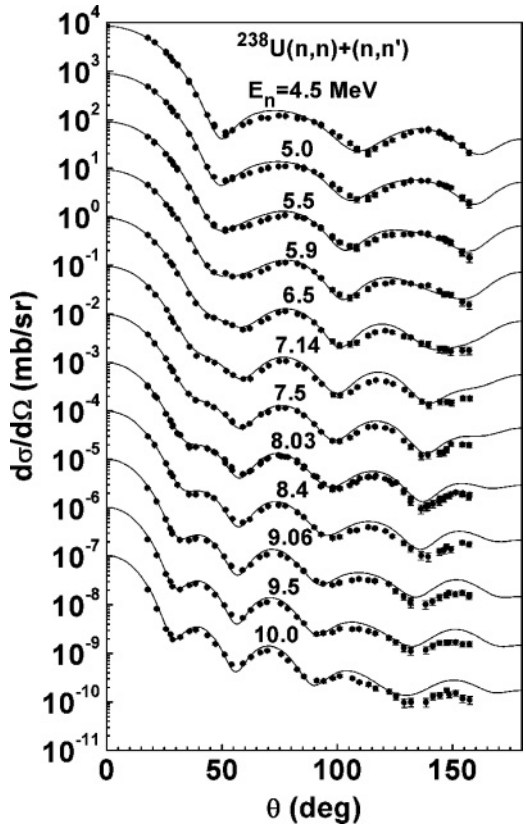

FIG. 12. Calculated elastic and inelastic scattering angular distributions of first, second, third, and fourth excited states (solid line) compared with experimental data [58] for $n + {}^{238}$U reactions. The results are offset by factors of $\times 10$, $\times 10^2$, $\times 10^3$, ...

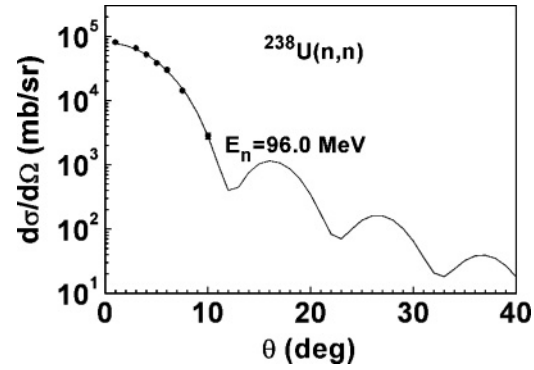

FIG. 13. Calculated elastic scattering angular distributions compared with experimental data [59] for $n + {}^{238}$U reactions at incident neutron energy 96.0 MeV.

[Eqs. (4) and (9)] increases with increasing incident nucleon energy. The contribution of the spin-orbit potential [Eq. (5)] of the optical model is small.

IV. THEORETICAL CALCULATIONS AND ANALYSIS

The experimental data of neutron total cross sections for $n + {}^{238,\text{nat}}$U and $n + {}^{232}$Th reactions were given in different laboratories, and experimental data of natural U and ^{238}U are basically in agreement with each other for energies below 300 MeV. The new total cross section experimental data [6] for $n + {}^{238}$U and $n + {}^{232}$Th reactions taken at the Weapons Neutron Research white neutron source facility and extended from 5 to 600 MeV are given by Abfalterer *et al.* [6] in 2001. The experimental data of neutron nonelastic scattering cross sections given for natural U, ^{235,238}U, and ^{239}Pu are below incident neutron energy 20 MeV, and there are no public experimental data for other actinides. There are some experimental data of neutron elastic scattering cross sections and elastic scattering angular distributions for ^{233,235,238}U, ^{232}Th, and ^{239}Pu below incident neutron energy 20.0 MeV, but inelastic scattering cross sections and inelastic scattering angular distributions for some excited states are included in some experimental data. There are some experimental data of neutron elastic scattering angular distributions for natural U

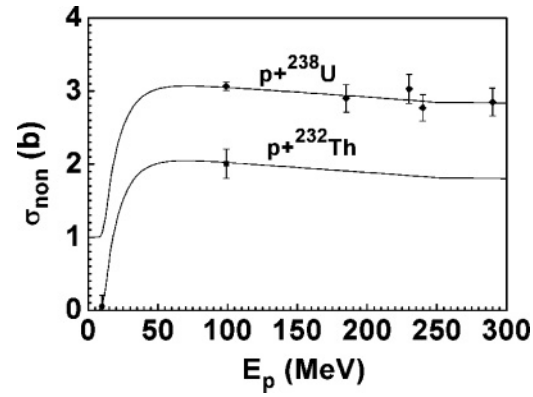

FIG. 14. Calculated reaction cross sections compared with experimental data [33,34] for $p + {}^{232}$Th and ^{238}U reactions. The results are offset by factors of $+1$ for $p + {}^{238}$U reactions.

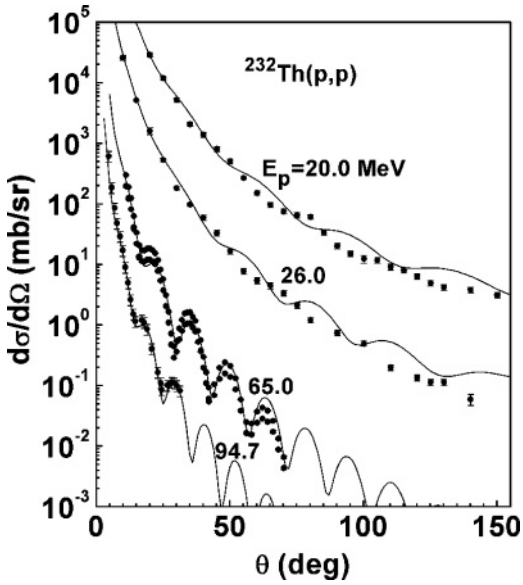

FIG. 15. Calculated elastic scattering angular distributions (solid line) compared with experimental data [61–63] for $p + {}^{232}$Th reactions. The results are offset by factors of $\times 10$, $\times 10^2$, and $\times 10^3$.

below incident neutron energy 120.0 MeV. The experimental data of proton reaction cross sections for natural U, ^{238}U, and ^{232}Th are below incident energy 350 MeV. Some experimental data of proton elastic scattering angular distributions and inelastic scattering angular distributions of some excited states for $p + {}^{235,238}$ U and ^{232}Th reactions are below incident proton energy 95.0 MeV.

The total cross sections for $n + {}^{232}$Th, $n + {}^{233,235,238}$U, $n + {}^{237}$Np, $n + {}^{239,240,242}$Pu, $n + {}^{241,243}$Am, $n + {}^{249}$Cm, $n + {}^{249}$Bk, and $n + {}^{249,250,251,252}$Cf reactions are calculated using the global optical model potential parameters from Table I.

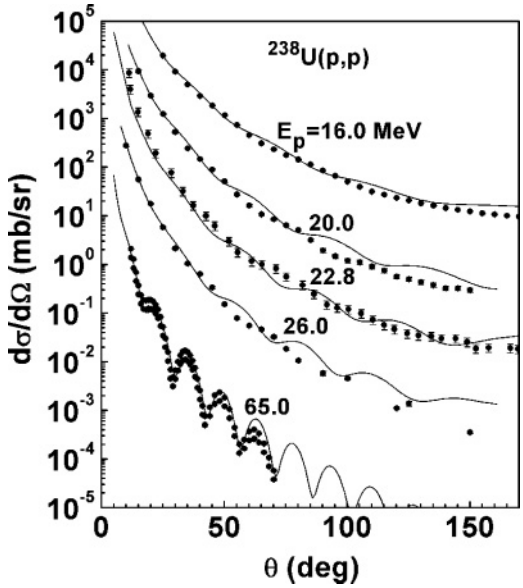

FIG. 16. Calculated elastic scattering angular distributions (solid line) compared with experimental data [61,62,64–66] for $p + {}^{238}$U reactions. The results are offset by factors of $\times 10$, $\times 10^2$, $\times 10^3$, and $\times 10^4$.

The comparisons of calculated results with experimental data [6–32] for some nuclei are given in Fig. 1. Figure 1 also shows the calculated results of total cross sections for $n + {}^{232}$Th and $n + {}^{233,235,238}$U reactions in incident neutron energy up to 300.0 MeV and for other nuclei up to 200.0 MeV. These results show that the theoretical values are in good agreement with the experimental data, and the theoretical values of some nuclei are larger than the experimental data for incident neutron energies from 0.1 to 1.0 MeV. The calculated results of total cross section for $n + {}^{232}$Th and $n + {}^{238}$U reactions are in good agreement with experimental data [6] taken at the weapons Neutron Research white neutron source facility. Since there are no experimental data of total cross sections above neutron energy 1.0 MeV, total cross sections for other nuclei are calculated and analyzed by the global optical model potential parameters obtained.

The calculated results of nonelastic scattering cross sections for $n + {}^{232}$Th, $n + {}^{235,238}$U, and $n + {}^{239}$Pu reactions are in good agreement with experimental data taken from EXFOR below neutron energy 20 MeV as showed in Fig. 2. Figure 2 also indicates that the calculated results of nonelastic scattering cross sections for $n + {}^{238}$U reactions above neutron energy 20 MeV are in reasonable agreement with experimental data [33,34] of proton reaction cross sections.

The calculated results of elastic scattering cross sections for $n + {}^{235,238}$U reactions are in good agreement with experimental data taken from EXFOR below neutron energy 20 MeV as shown in Fig. 3. The calculated results of elastic scattering cross sections for $n + {}^{232}$Th, ^{237}U, and ^{239}Pu reactions pass through some existing experimental data below incident neutron energy 14.0 MeV. There are no experimental data for other nuclei up to now from the published literature.

The comparisons of calculated results of elastic scattering angular distribution with experimental data for ^{238}U are given in Fig. 4. The calculated results are in good agreement with experimental data [35–37]. The calculated results of elastic scattering angular distribution for $n + {}^{232}$Th, ^{233,235}U, ^{237}Np, and ^{239}Pu reactions are also in good agreement with the experimental data.

Since the actinides are deformed nuclei and the energy of ground state rotational bands is small, it is almost impossible to separate neutron inelastic scattering data from elastic scattering data experimentally for the actinide nuclei at incident energies above several MeV. The experimental data of neutron angular distribution including neutron elastic scattering and inelastic scattering of the first, second, third, and fourth excited states of different nuclei were given in different laboratories, respectively. Because the contributions of neutron inelastic scattering angular distribution are important in total neutron angular distribution, the calculated results of total neutron angular distributions include the contribution of inelastic scattering angular distributions of the first to fourth excited states of the target nucleus.

The inelastic scattering angular distributions for the first, second, third and fourth excited states of ^{232}Th, ^{233,235,238}U, and ^{239,242}Pu are calculated. The calculated results are in good agreement with experimental data. The comparisons of calculated results of inelastic scattering angular distribution of first and second excited states with experimental data [36,37]

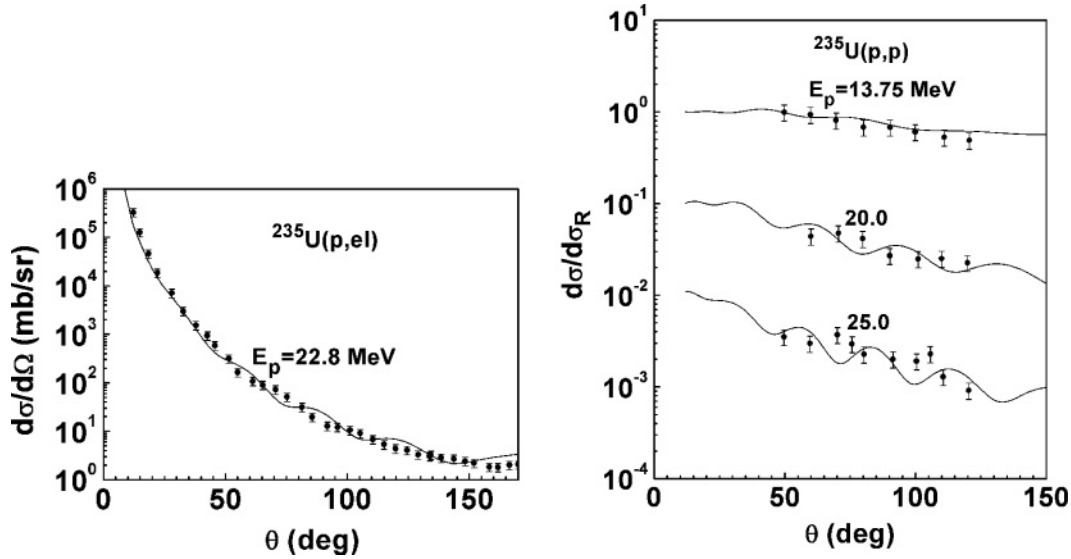

FIG. 17. Calculated elastic scattering angular distributions (solid line) compared with experimental data [66,67] for $p + {}^{235}$U reactions. The results are offset by factors of $\times 10$ and $\times 10^2$.

for ^{238}U are only given in Figs. 5 and 6, respectively. The inelastic scattering angular distributions for the first and second excited states of ^{232}Th, ^{235}U, and ^{239}Pu are also in good agreement with experimental data [36] at incident neutron energy 3.4 MeV.

The comparisons of the calculated results including elastic scattering angular distribution and inelastic scattering angular distribution of the first, second, third, and fourth excited states with experimental data [35–58] for $n + {}^{232}$Th, ^{235,238}U, and ^{239}Pu reactions are given in Figs. 7–10. The energy and spin-parity of the first, second, third, and fourth excited states are 0.0494 2+, 0.1621 4+, 0.3332 6+, and 0.5569 8+ for ^{232}Th; 0.0449 2+, 0.1484 4+, 0.3072 6+, and 0.5183 8+ for ^{238}U; and 0.0079 1.5+, 0.0573 2.5+, 0.0757 3.5+, and 0.1638 4.5+ for ^{239}Pu. The energy and spin-parity of the excited states are 0.0462 4.5−, 0.1030 5.5−, 0.1707 6.5−, and 0.2491 7.5− for ^{235}U. The calculated results are in good agreement with experimental data. Since the experimental data of elastic scattering angular distributions at some incident energies are given in Figs. 7–10, the calculated results indicate that the contributions of inelastic scattering angular distribution of the first, second, third, and fourth excited states of ^{232}Th, ^{235}U, ^{238}U, and ^{239}Pu are included in those experimental data.

The comparisons of calculated results including elastic scattering angular distribution and inelastic scattering angular

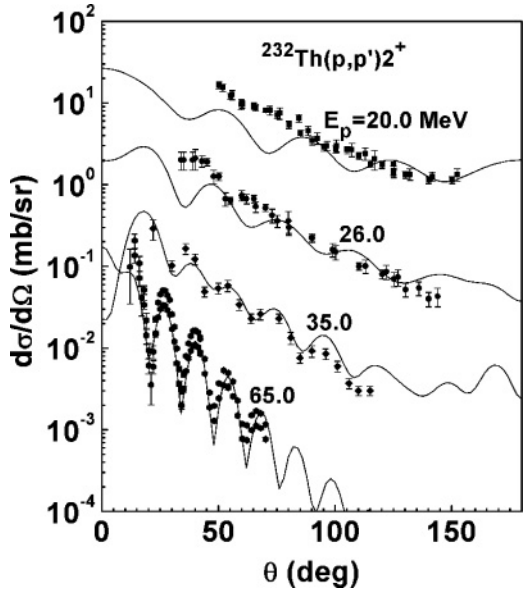

FIG. 18. Calculated inelastic scattering angular distributions of the first excited state (solid line) compared with experimental data [61,62,64,68] for $p + {}^{232}$Th reactions. The results are offset by factors of $\times 10$, $\times 10^2$, and $\times 10^3$.

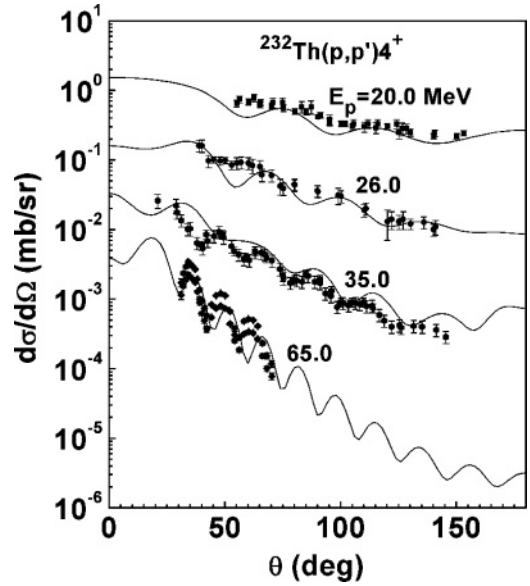

FIG. 19. Calculated inelastic scattering angular distributions of the second excited state (solid line) compared with experimental data [61,62,64,68] for $p + {}^{232}$Th reactions. The results are offset by factors of $\times 10$, $\times 10^2$, and $\times 10^3$.

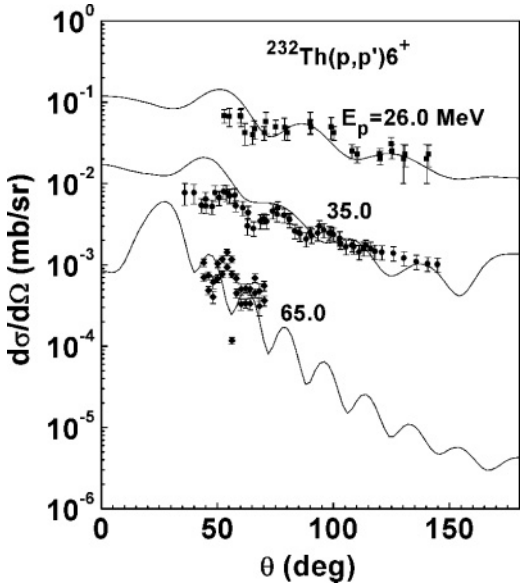

FIG. 20. Calculated inelastic scattering angular distributions of the third excited state (solid line) compared with experimental data [61,62,64,68] for $p + {}^{232}$Th reactions. The results are offset by factors of $\times 10$ and $\times 10^2$.

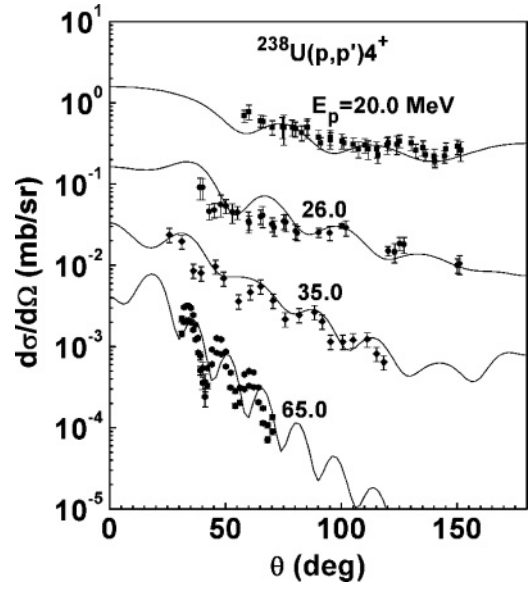

FIG. 22. Calculated inelastic scattering angular distributions of the second excited state (solid line) compared with experimental data [61,62,64,68] for $p + {}^{238}$U reaction. The results are offset by factors of $\times 10$, $\times 10^2$, and $\times 10^3$.

distribution of the first, second, third, and fourth excited states with experimental data taken from Ref. [58] for ^{232}Th and ^{238}U are given in Figs. 11 and 12, respectively. The calculated results are in good agreement with experimental data.

The experimental data of neutron elastic scattering angular distributions for natural U in incident neutron energy from 18 to 120.0 MeV are given in Refs. [59,60]. The calculated results of elastic scattering angular distributions for $n + {}^{233,235,238}$U reactions are in good agreement with experimental data. Figure 13 only gives the comparisons of calculated results with experimental data [59] for ^{238}U at incident neutron energy 96.0 MeV.

The comparisons of calculated results of proton reaction cross sections with experimental data taken from Refs. [33,34] for $p + {}^{232}$Th and ^{238}U reactions are given in Fig. 14. The calculated results are in good agreement with experimental data. Since the experimental data taken from Refs. [33,34] are from $p +$ U reactions, the calculated results of reaction cross

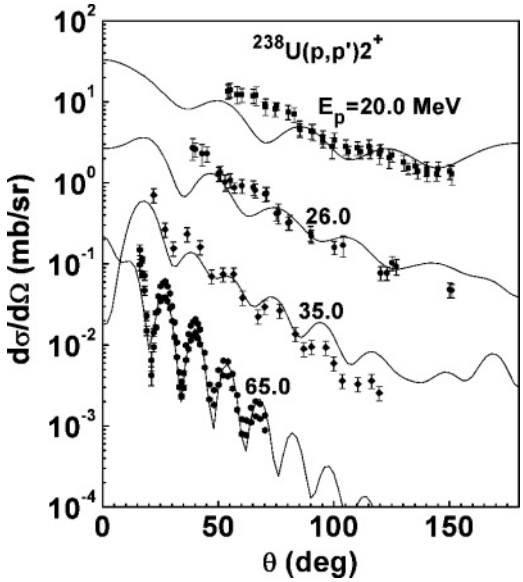

FIG. 21. Calculated inelastic scattering angular distributions of the first excited state (solid line) compared with experimental data [61,62,64,68] for $p + {}^{238}$U reactions. The results are offset by factors of $\times 10$, $\times 10^2$, and $\times 10^3$.

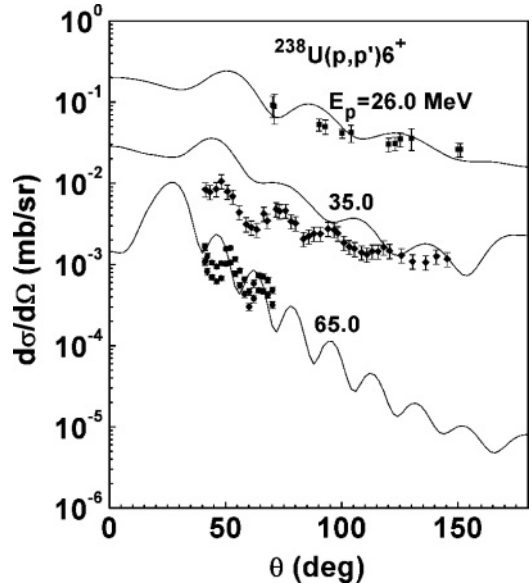

FIG. 23. Calculated inelastic scattering angular distributions of the third excited state (solid line) compared with experimental data [61,62,64,68] for $p + {}^{238}$U reactions. The results are offset by factors of $\times 10$ and $\times 10^2$.

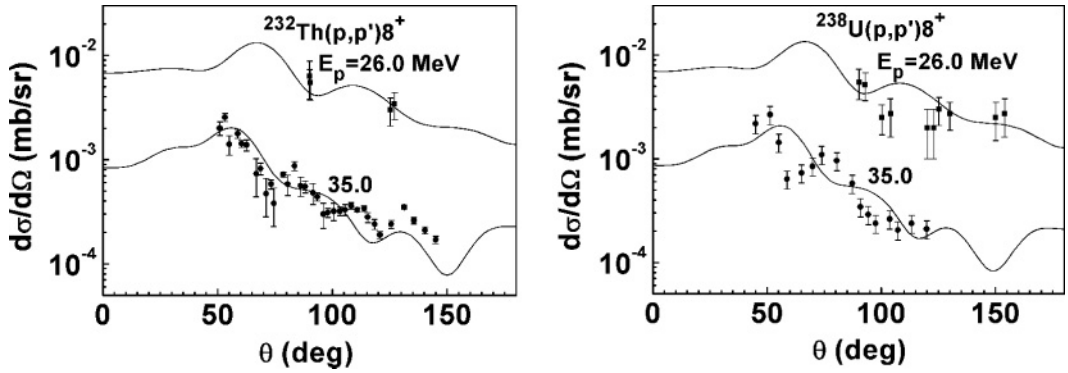

FIG. 24. Calculated inelastic scattering angular distributions of the fourth excited state (solid line) compared with experimental data [61,68] for $p + {}^{238}$Th and ^{238}U reactions. The results are offset by factors of $\times 10$.

sections for $p + {}^{233,235,237}$U reactions are also in reasonable agreement with experimental data. There is no experimental data for other nuclei up to now from the published literature.

Figures 15–17 give the comparisons of calculated results of elastic scattering angular distributions with experimental data [61–67] for $p + {}^{232}$Th and ^{235,238}U reactions in incident proton energies from 13.0 to 95.0 MeV; the calculated results fit experimental data very well for all energy points.

Figures 18–24 give the comparisons of calculated results of inelastic scattering angular distributions with experimental data [61,62,64,68] for $p + {}^{232}$Th and ^{238}U reactions in incident proton energies from 20.0 to 65.0 MeV. The calculated results of $p + {}^{232}$Th reactions fit experimental data well for all excited states and incident proton energy points. The calculated results of the first and second excited states of $p + {}^{238}$U reactions fit experimental data well for all incident proton energies. Figures 23 and 24 show that the calculated results of the third and fourth excited state of $p + {}^{238}$U reactions are basically in agreement with experimental data.

We can see that a set of global neutron and proton optical model potential parameters obtained from this work gives a good description of measured elastic and inelastic scattering angular distributions for neutron- and proton-induced reactions. The results for other nuclei are calculated by the global optical model potential, since the optical model potential depths is dependent on the mass number A and the neutron number N of the target.

V. CONCLUSIONS

In this work we have presented a set of neutron and proton global optical model potential parameters for actinide (the charge number range is $89 \leqslant Z \leqslant 100$ and the mass range is $220 \leqslant A \leqslant 260$) and the nucleon energy up to 300 MeV by using the experimental data of neutron total reaction cross sections, nonelastic cross sections, elastic cross sections, and angular distributions and proton total reaction cross sections and elastic scattering angular distributions of ^{232}Th and ^{238}U. The optical model potentials are based on a smooth, unique functional form for the energy dependence of the potential depths and on physically constrained geometry parameters. The experimental data and the calculated results by global optical model potential are compared and analyzed. The excellent overall agreement obtained between calculations and experimental data are generally observed. The experimental data of inelastic scattering angular distributions are also well described by the global optical model potential. The potential developed in this article may find direct application in theoretical nuclear model calculations and experiment analysis.

ACKNOWLEDGMENTS

This work is part of the National Basic Research Program of China (973 Program). The program is entitled Key Technology Research of Accelerator Driven Sub-critical System for Nuclear Waste Transmutation and is supported by the China Ministry of Science and Technology under Contract No. 2007CB209903. This work is a part of IAEA Coordinated Research Projects (CRPs) on Analytical and Experimental Benchmark Analyses of Accelerator Driven Systems (ADS) under Contract No. 13390/R2 and on Minor Actinides Neutron Cross Section Data for Closed Fuel Reactor Concepts under Contract No. 14383/R1.

[1] A. J. Koning and J. P. Delaroche, Nucl. Phys. **A713**, 231 (2003).
[2] F. D. Becchetti and G. W. Greenlees, Phys. Rev. **182**, 1190 (1969).
[3] P. D. Kunz, Distorted Wave Code DWUCK4, University of Colorado, 1994.
[4] Qingbiao Shen, Nucl. Sci. Eng. **141**, 78 (2002).
[5] B. Alder, S. Fernbach, and M. Rotenberg, *Methods in Computational Physics* (Academic Press, New York/London, 1966), Vol. 6, p. 1.
[6] W. P. Abfalterer, F. B. Bateman, F. S. Dietrich, R. W. Finlay, R. C. Haight, and G. L. Morgan, Phys. Rev. C **63**, 044608 (2001).
[7] D. G. Foster Jr. and D. W. Glasgow, Phys. Rev. C **3**, 576 (1971).
[8] J. F. Whalen and A. B. Smith, Nucl. Sci. Eng. **67**, 129 (1978).

[9] W. P. Poenitz, J. F. Whalen, and A. B. Smith, Nucl. Sci. Eng. **78**, 333 (1981).
[10] T. Iwasaki, M. Baba, K. Hattori, K. Kanda, S. kamata, and N. Hirakawa, NEANDC(J)-75, 1981.
[11] L. Green and J. A. Mitchell, WAPD-TM-1073 (1973).
[12] W. P. Poenitz, J. F. Whalen, P. Guenther, and A. B. Smith, Nucl. Sci. Eng. **68**, 358 (1978).
[13] R. J. Schneider and A. M. Cormack, Nucl. Phys. **A119**, 197 (1968).
[14] W. P. Poenitz and J. F. Whalen, ANL-NDM-80 (1983).
[15] P. H. Bowen, J. P. Scanlon, G. H. Stafford, J. J. Thresher, and P. E. Hodgson, Nucl. Phys. **22**, 640 (1961).
[16] J. Franz, H. P. Grotz, L. Lehmann, E. Roessle, H. Schmitt, and L. Schmitt, Nucl. Phys. **A490**, 667 (1988).
[17] R. B. Schwartz, R. A. Schrack, and H. T. Heaton II, Nucl. Sci. Eng. **54**, 322 (1974).
[18] F. L. Green, K. A. Nadolny, and P. Stoler, USNDC-9, 170, (1973).
[19] K. H. Boeckhoff, A. Dufrasen, G. Rohr, and H. Weigmann, J. Nucl. Energy **26**, 91 (1972).
[20] J. Cabe and M. Cance, CEA-R-4524 (1973).
[21] J. F. Whalen and A. B. Smith, ANL-7710, 9 (1971).
[22] S. H. Hayes, P. Stoler, J. M. Clement, and C. A. Goulding, Nucl. Sci. Eng. **50**, 243 (1973).
[23] M. Baba, K. Nomoto, K. Kanda, N. Hirakawa, J. Mitsui, and T. Momota, EANDC(J)-30, 66 (1973).
[24] G. F. Auchampaugh *et al.*, Phys. Rev. C **29**, 174 (1984).
[25] A. A. Lychagin, B. V. Zhuravlev, V. I. Trykova, and V. G. Demenkov, JINR-E3-97-213, 355 (1997).
[26] R. Spencer, J. A. Harvey, N. W. Hill, and L. W. Weston, Nucl. Sci. Eng. **96**, 318 (1987).
[27] D. B. C. B. Syme, J. D. Kellie, J. McKeown, S. J. Hall, and G. I. Crawford, Ann. Nucl. Energy **1**, 305 (1974).
[28] A. B. Smith, P. Guenther, and J. Whalen, J. Nucl. Energy **27**, 317 (1973).
[29] K. A. Nadolny, F. L. Green, and P. Stoler, USNDC-9, 170 (1973).
[30] A. B. Smith, J. F. Whalen, and P. Lambropoulos, Nucl. Sci. Eng. **47**, 19 (1972).
[31] M. S. Moore, P. W. Lisowski, G. L. Morgan, G. F. Auchampaugh, and R. E. Shamu, in *Proceedings of Conference on Nuclear Cross Sections for Technology*, Knoxville, 1979, p. 703.
[32] T. W. Phillips and R. E. Howe, Nucl. Sci. Eng. **69**, 375 (1979).
[33] G. P. Millburn, W. Birnbaum, W. E. Crandall, and L. Schecter, Phys. Rev. **95**, 1268 (1954).
[34] P. Kirkby and W. T. Link, Can. J. Phys. **44**, 1847 (1966).
[35] A. V. Murzin *et al.*, Ann. Energy **62**, 192 (1987).
[36] G. Haouat, J. Lachkar, C. H. Lagrange, J. Jay, J. Sigaud, and Y. Patin, Nucl. Sci. Eng. **81**, 491 (1982).
[37] L. E. Beghian *et al.*, Nucl. Sci. Eng. **69**, 191 (1979).
[38] R. Batchelor, W. B. Gilboy, and J. H. Towle, Nucl. Phys. **65**, 236 (1965).
[39] C. I. Hudson Jr, W. S. Walker, and S. Berko, Phys. Rev. **128**, 1271 (1962).
[40] S. C. Buccino, C. E. Hollandsworth, and P. R. Bevington, Z. Phys. **196**, 103 (1966).
[41] V. I. Popov, in *Soviet Progress in Neutron Physics* (Consultants Bureau, New York, 1963), p. 224.
[42] G. C. Goswami, J. J. Egan, G. H. R. Kegel, A. Mittler, and E. Sheldon, Nucl. Sci. Eng. **100**, 48 (1988).
[43] G. Dagge, W. Grum, J. W. Hammer, K.-W. Hoffmann, and G. Schreder, Phys. Rev. C **39**, 1768 (1989).
[44] T. Iwasaki *et al.* (private communication, 1981).
[45] L. F. Hansen, B. A. Pohl, C. Wong, R. C. Haight, and C. H. Lagrange, Phys. Rev. C **34**, 2075 (1986).
[46] G. C. Goswami, thesis, 1986, Exfor No. 13506001.
[47] H.-H. Knitter, M. M. Islam, and M. Coppola, Z. Phys. **257**, 108 (1972).
[48] R. C. Allen, R. B. Walton, R. B. Perkins, R. A. Olson, and R. F. Taschek, Phys. Rev. **104**, 731 (1956).
[49] R. Batchelor and K. Wyld, AWRE-O-55/69 (1969), Exfor No. 20036001.
[50] J. Annand and R. Galloway, J. Phys. G **11**, 1341 (1985).
[51] G. V. Anikin and I. I. Kotukhov, Yad. Fiz. **12**, 1121 (1970).
[52] Q. Bujia, T. Hongqing, Z. Zuying, S. Jun, K. Zunjuan, S. Qingchang, and X. Haihong, in Symposium on Fast Neutron Physics, Beijing, 1991, p. 32.
[53] J. Voignier, CEA-R-3503 (1968).
[54] S. Guanren *et al.*, Chinese Nucl. Phys. **6**, 193 (1984).
[55] B. Y. Guzhovskiy, Atomnaya Energiya **11**, 395 (1961).
[56] G. Yue, M. O'Connor, J. J. Egan, and G. H. R. Kegel, Nucl. Sci. Eng. **122**, 366 (1996).
[57] M. Coppola and H.-H. Knitter, Z. Phys. **232**, 286 (1970).
[58] A. B. Smith and S. Chiba, Ann. Nucl. Energy **23**, 459 (1996).
[59] G. L. Salmon, Nucl. Phys. **21**, 15 (1960).
[60] P. H. Bowen *et al.*, Nucl. Phys. **40**, 186 (1963).
[61] L. F. Hansen, I. D. Proctor, D. W. Heikkinen, and V. A. Madsen, Phys. Rev. C **25**, 189 (1982).
[62] Y. Takeuchi, H. Sakaguchi, M. Nakamura, T. Ichihara, M. Yosoi, M. Ieiri, and S. Kobayashi, Phys. Rev. C **34**, 493 (1986).
[63] G. Gerstein, J. Niederer, and K. Strauch, Phys. Rev. **108**, 427 (1957).
[64] T. Ichihara, H. Sakaguchi, M. Nakamura, M. Yosoi, M. Ieiri, Y. Takeuchi, H. Togawa, T. Tsutsumi, and S. Kobayashi, Phys. Rev. C **36**, 1754 (1987).
[65] R. Varner, Phys. Rep. **201**, 57 (1991).
[66] C. B. Fulmer, Phys. Rev. **116**, 418 (1959).
[67] J. R. Boyce, Phys. Rev. C **10**, 231 (1974).
[68] C. H. King, J. E. Finck, G. M. Crawley, J. A. Nolen Jr., and R. M. Ronningen, Phys. Rev. C **20**, 2084 (1979).